Soft Matter

PAPER

View Article Online
View Journal | View Issue

Cite this: *Soft Matter*, 2018, **14**, 9005

Cylindrical nematic liquid crystal shell: effect of saddle-splay elasticity†

Arman Javadi,‡[a] Jonghee Eun[a] and Joonwoo Jeong *[ab]

Received 7th September 2018,
Accepted 19th October 2018

DOI: 10.1039/c8sm01829d

rsc.li/soft-matter-journal

This study introduces cylindrical nematic liquid crystal (LC) shells. Shells as confinement can provide soft matter with intriguing topology and geometry. Indeed, in spherical shells of LCs, rich defect structures have been reported. Avoiding the inherent Plateau–Rayleigh instability of cylindrical liquid–liquid interfaces, we realize the cylindrical nematic LC shell by two different methods: the phase separation in the nematic–isotropic coexistence phase and a cylindrical cavity with a glass rod suspended in the middle. Specifically, the director configurations of lyotropic chromonic LCs (LCLCs) in the cylindrical shell and their energetics are investigated theoretically and experimentally. Unusual elastic properties of LCLCs, *i.e.*, a large saddle-splay modulus, and a shell geometry with both concave and convex curvatures, result in a double-twist director configuration.

The geometry and topology of confinement determine the director configurations of confined liquid crystals (LCs) and topological defects therein. Notably, the curvatures of a confining geometry as boundary conditions directly affect the director configuration of the ground state.[1,2] This is because the director configuration tries to minimize the surface anchoring energy as well as the bulk elastic free energy, *i.e.*, minimizing the total free energy. A variety of confining geometries have been investigated and adopted for applications. For example, nematic LCs can be sandwiched between two planar substrates or put into droplets, capillaries, and tori.[1,3–13] Even, particles and droplets can be embedded into LCs to form LC colloids.[14–19]

LC shells have provided unique confinement regarding the geometry and topology.[9,13,20–31] LC shells can form when LCs with single or multiple immiscible inclusions are surrounded by another immiscible medium. They are often implemented by microfluidics-generated multiple emulsions, *e.g.*, water-in-LC-in-water (W/LC/W) droplets. The LC shell in a W/LC/W droplet is topologically distinct from the LC droplet dispersed in water. Additionally, it encounters both concave and convex water–LC interfaces with different radii of curvature, and the surface anchoring at each interface can be controlled independently. This results in intriguing topological defects and director configurations according to shell thickness, anchoring conditions, and LC phases. Despite the exciting aspects of the shell geometry, a stable shell has been realized only in the form of spherical droplets.

Here we report the director configurations of nematic lyotropic chromonic LCs (LCLCs) confined in a cylindrical shell with planar anchoring at both interfaces. We also introduce experimental methods to make the cylindrical shells. In addition to the uniqueness of the spherical shell, the cylindrical shell renders anisotropic principal curvatures that can give rise to a curvature-induced surface alignment owing to a saddle-splay modulus K_{24}.[12,32] The large K_{24} will tend to align the surface directors along the circumference of the cylinder at the concave interface of the cylindrical shell. At the convex interface, the directors favor the alignment along the capillary axis of zero curvature. For instance, LCLCs having unusual elastic properties,[33–39] *i.e.*, a very small twist modulus, and an unprecedentedly large saddle-splay modulus, exhibit an escaped-twist, *i.e.*, double-twist, director configuration in a cylindrical cavity with a degenerate planar anchoring.[40,41] Here in the cylindrical shell with both concave and convex interfaces, we investigated experimentally and theoretically the director configuration accompanied by the topological defects due to spontaneous chiral symmetry breaking.

Materials and methods

Sample preparation

We used disodium cromoglycate (DSCG) as our model LCLC.[42,43] DSCG was purchased from Sigma-Aldrich at purities of >95% and used as received. By dissolving DSCG into deionized water (18.2 MΩ cm), we made nematic DSCG solutions of desired concentrations ranging from 12.0 to 14.0% (wt/wt).

[a] *Department of Physics, Ulsan National Institute of Science and Technology (UNIST), Ulsan 44919, Republic of Korea. E-mail: jjeong@unist.ac.kr*
[b] *Center for Soft and Living Matter, Institute for Basic Science, Ulsan 44919, Republic of Korea*

† Electronic supplementary information (ESI) available. See DOI: 10.1039/c8sm01829d

‡ Present address: Department of Materials Science and Engineering, Shiraz University, Iran.

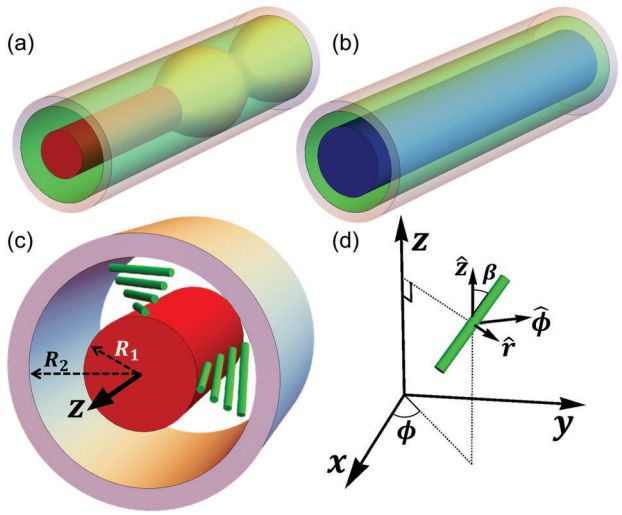

Fig. 1 Schematic diagrams of cylindrical nematic LC shells and double-twist director configuration. The cylindrical shell is formed by (a) suspending a cylindrical rod in a capillary tube and (b) preferential wetting of a nematic phase on the capillary tube in the nematic–isotropic coexistence phase. Green regions in (a and b) correspond to nematic LC phases. The red cylinder in (a) is the suspending glass rod and it is partially coated by soft silicone gel shown as bumpy drops wetting one end of the red rod. The blue cylinder in (b) represents a liquid thread by the isotropic phase in the coexistence phase. (c) A schematic diagram showing the double-twist director configuration in the cylindrical shell. The red cylinder of radius R_1 is suspended in the middle of the capillary tube of radius R_2. The z axis of the cylindrical coordinates is the axis of symmetry of the capillary tube. The gap between the rod and tube is filled with nematic LC of which directors are shown as green rods. The directors exhibit twist deformation along the direction of radius. (d) A schematic diagram showing the Cartesian and cylindrical coordinate system. The angle between the director (green) and the unit vector $\hat{z}$ is the twist angle β; note that the directors in the double-twist configuration do not have radial components along $\hat{r}$.

We confined nematic LCLCs into a cylindrical shell using two different methods. First, the nematic–isotropic coexistence phase in a cylindrical cavity spontaneously forms the nematic shell and the isotropic core. When we lower the temperature of the LCLC in a circular capillary tube from the isotropic phase to the coexistence phase, the nematic phase starts to grow from the walls, forming an isotropic cylinder in the middle of the capillary; the green and blue regions in Fig. 1(a and b) depict the nematic and isotropic phases, respectively. Borosilicate glass capillaries (Vitrotubes™, Vitrocom) of the inner diameter of 100 and 200 μm were used as received. In certain circumstances, this core–shell structure can be stable without Plateau–Rayleigh instability, for up to 40 minutes at a fixed temperature. For instance, after infiltrating the capillary tube with the 14.0% (wt/wt) nematic DSCG, we melted the LCLC entirely into the isotropic phase and then decreased the temperature from 40 °C to 29.5 °C at the rate of 2.0 °C min^{-1} to make an approximately 10 μm-thick nematic film in the capillary of 100 μm diameter. We controlled the temperature to change the volume ratio between the isotropic and nematic phase and the resulting thickness of the nematic shell. The lower the final temperature is, the thicker the nematic shell is. The sample was kept and observed in the final temperature until Plateau–Rayleigh instability occurs.

Second, we put a cylindrical glass rod of diameter 100 μm (Glass rods made of borosilicate glass 3.3, Hilgenberg) into a capillary tube with the inner diameters of 200 μm ± 10%. To suspend the glass rod at the center of the tube, we coated some part of the rod with soft silicone gel (Sylgard 527, Dow Corning) by dip coating and thermal curing per the manufacturer's directions. Due to the instability of a liquid film coating a vertical cylindrical rod, the liquid film destabilizes into an array of drops.[44] The maximum height of these drops can be controlled by changing the initial film thickness on the rod. Since these drops are soft and rotationally symmetric, the coating as a soft spacer can place the glass rod in the middle of the tube, as sketched in Fig. 1(a). Before assembling the rod and tube completely, the gap between them was filled with nematic LCLC by capillarity. The sealed sample was kept at 45.0 °C for 10 minutes, and then was relaxed at 23.0 °C over 4 hours before observation. Note that all capillary tubes were put on glass slides and both ends were sealed with epoxy glue to minimize the evaporation of water.

Optical microscopy

A cover-slip was placed on top of the capillary tubes. The volume between the glass slide and cover-slip was filled with a refractive index matching oil (refractive index = 1.474 at wavelength 589.3 nm, Cargile). All optical microscope images were taken using an Olympus BX 53P equipped with a color CCD (Infinity3-6UR, Lumenera) under quasi-monochromatic illumination (center wavelength = 660 nm, FWHM = 25 nm; LED4D067, Thorlabs). A polarizer and an analyzer can be rotated freely with respect to the sample. For phase retardation experiments, a full-wave plate (optical path difference = 550 nm, Olympus) was placed in front of the analyzer.

Characterization of the director configurations using Jones calculus

We applied Jones calculus to simulate the optical textures of the cylindrical nematic LC shells between crossed polarizers thus to characterize the director configuration.[6,45] Given the directions of polarizers, a director field model, refractive indices, an illumination wavelength, the thickness of a shell, and the diameter of a capillary tube, we calculate the transmittance of the light ray along the diameter between polarizers. This calculation through the central region of the capillary can be extended to simulate 2D optical textures of the sample in polarized optical microscopy, adopting a parallel ray approximation, *i.e.*, ignoring the effects of refraction, reflection, and diffraction.

To characterize the director configurations, we first measured experimental transmittance profiles at the central region while rotating a polarizer and an analyzer in the opposite direction. The experimental profiles were compared to the numerically generated transmittance profiles to find best matching parameters including birefringence Δn and the twist angles at the inner and outer interfaces of the shell, respectively. Specifically, assuming that the twist angle is changing linearly with respect to the radius, we numerically calculated transmittance profiles scanning through a reasonable range for each parameter in the set: the birefringence, the twist angle at

the inner interface, and the twist angle at the outer interface. Then, the least square method found the best matches for the experimental transmittance profile. Negative values for the twist angle were also scanned to distinguish the different handednesses. Additionally, to resolve the degeneracy problem in the transmittance profile, the numerically calculated 2D transmittance images were compared to the experimental polarized optical microscopy (POM) image. Finally, we select the one parameter-set having the best image match with the experimental image.

Results and discussion

Theory

We calculate the equilibrium director configuration by the calculus of variations, *i.e.*, solving Euler–Lagrange equations. As shown in the cylindrical shell geometry of Fig. 1(c), a cylinder of radius R_1 is located in the middle of a larger capillary tube of an inner radius R_2, and the LC fills the shell volume between the two cylinders. The boundary conditions on both inner and outer walls are degenerate planar anchoring.

To find the equilibrium director configuration, we minimize the Oseen–Frank elastic free energy

$$F = \int \mathrm{d}^3x \left[\frac{1}{2}K_1(\nabla\cdot\bar{\mathbf{n}}) + \frac{1}{2}K_2(\bar{\mathbf{n}}\cdot\nabla\times\bar{\mathbf{n}})^2 + \frac{1}{2}K_3(\bar{\mathbf{n}}\times\nabla\times\bar{\mathbf{n}})^2 - \frac{1}{2}K_{24}\nabla\cdot(\bar{\mathbf{n}}\times\nabla\times\bar{\mathbf{n}} + \bar{\mathbf{n}}\nabla\cdot\bar{\mathbf{n}})\right], \quad (1)$$

where $\bar{\mathbf{n}}$ is the nematic director. K_1, K_2, K_3 and K_{24} are the splay, twist, bend and saddle-splay elastic constants, respectively. Using cylindrical coordinates, with the z axis along the capillary axis of symmetry, we assume

$$\bar{\mathbf{n}} = \sin\beta(r)\hat{\phi} + \cos\beta(r)\hat{\mathbf{z}}, \quad (2)$$

where $\beta(r)$ is the twist angle with respect to the z axis at radius r from the center ($R_1 \le r \le R_2$), as shown in Fig. 1(d). Note that the azimuthally symmetric director has no $\hat{\mathbf{r}}$ component satisfying the planar anchoring at both the inner and outer walls. After putting eqn (2) into eqn (1), and minimizing the free energy using the calculus of variations, we find the following nonlinear differential equation of the second order for $\beta(\rho)$

$$\rho^2\beta'' + \rho\beta' = \frac{1}{2}\sin 2\beta\cos 2\beta + \frac{2}{k_2}\sin^3\beta\cos\beta, \quad (3)$$

where $k_2 = K_2/K_3$, and primes denote differentiation with respect to $\rho = r/R_2$. We also find two boundary conditions at the inner and outer walls for determining $\beta(\rho_1 = R_1/R_2)$ and $\beta(\rho_2 = R_2/R_2 = 1)$

$$k_2\rho_i\left(\frac{\mathrm{d}\beta}{\mathrm{d}\rho}\right)_{\rho=\rho_i} = (k_{24} - k_2)\sin\beta(\rho_i)\cos\beta(\rho_i), \quad i = 1, 2. \quad (4)$$

where $k_{24} = K_{24}/K_3$. As shown in eqn (3) and (4), the splay deformation plays no role in the director configuration. Note also that for $\rho_1 = 0$, *i.e.*, no inner cylinder, the boundary condition (eqn (4)) gives $\beta(\rho = 0) = 0$. In other words, the escaped-twist director configuration[40,41,46] in a cylindrical cavity becomes just a particular case of the general cylindrical shell structure as expected.

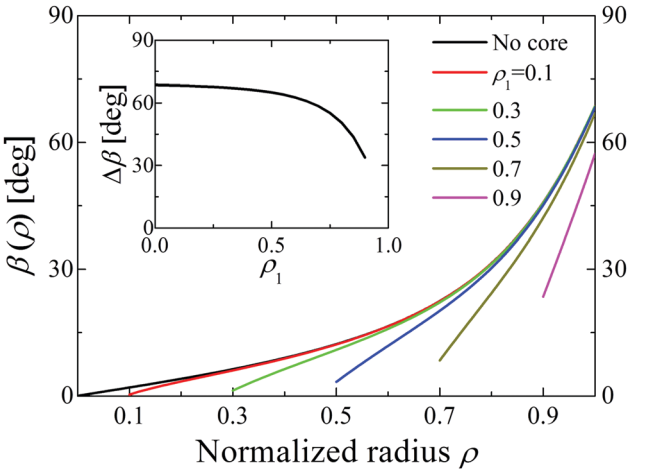

Fig. 2 A numerically calculated twist angle profile in the double-twist director configuration. The twist angle β is plotted as a function of the normalized radius $\rho = r/R_2$ according to different normalized inner shell radius $\rho_1 = R_1/R_2 = 0.1,\ldots,0.9$ when $k_2 = \frac{1}{30}$ and $k_{24} = \frac{1}{2}$, *i.e.*, the approximate elastic constants of 14.0% (wt/wt) nematic DSCG at 23.0 °C. The inset shows the amount of twist $\Delta\beta = |\beta_2 - \beta_1|$ according to different ρ_1.

We calculated the twist angle profile $\beta(\rho)$ in the range $\rho \in [\rho_1,1]$ according to ρ_1, k_2 and k_{24}. Specifically, we solved eqn (3) and (4) using the shooting method to solve differential equations. Fig. 2 shows representative results $\beta(\rho)$ of 14.0% (wt/wt) nematic DSCG of $k_2 = \frac{1}{30}$ and $k_{24} = \frac{1}{2}$ according to various ρ_1. We find that, as in the cylinder case,[40] $K_{24} \le 2K_2$ also give a trivial parallel-axial configuration, $\beta(\rho) = 0$, in the cylindrical shell (see the ESI† for the proof). Namely, as long as K_{24} surpasses $2K_2$, the ground state of the cylindrical nematic shell is the double-twist configuration regardless of the thickness and curvatures of the shell. Note that the critical value of K_{24} for the chiral symmetry breaking in tori is slightly smaller than $2K_2$.[32]

The competition between the saddle-splay and twist elastic constants determines the twist angles at the inner and outer wall, *i.e.*, $\beta(\rho_1) = \beta_1$ and $\beta(\rho_2 = 1) = \beta_2$. First, the saddle-splay constant K_{24} aligns the surface directors according to the principal curvatures of the inner and outer walls of the shell, and this results in the double-twist configuration.[40,41] A twist angle $\beta_2 = 90°$ minimizes the saddle-splay term at the outer wall because the saddle-splay term favors alignment of the surface directors along the direction of the largest principal curvature, *i.e.*, the direction of the circumference, according to eqn (5).[32]

$$F_{24} = -\frac{1}{2}K_{24}\int \mathrm{d}^3x\nabla\cdot(\bar{\mathbf{n}}\times\nabla\times\bar{\mathbf{n}} + \bar{\mathbf{n}}\nabla\cdot\bar{\mathbf{n}}) = -\frac{1}{2}K_{24}\int \mathrm{d}S(\kappa_1 n_1^2 + \kappa_2 n_2^2) \quad (5)$$

Note that the surface normal vector used in eqn (5) is pointing inward. κ_1 and κ_2 are two principal curvatures at the surface, and n_1 and n_2 are the vector components along the directions of the curvatures in the plane of the surface, respectively. In the same vein, the saddle-splay term at the inner wall becomes the minimum when $\beta_1 = 0^\circ$, *i.e.*, alignment along the capillary axis, because the curvature along the circumference at the inner wall is negative. Namely, the saddle-splay elasticity works like a curvature-induced azimuthal anchoring, and the cylindrical shell geometry with both convex and concave interfaces resembles the planar twisted nematic cell. Simultaneously, the twist term resists the 90-degree-twisting. This competition between the saddle-splay and twist elasticity leads to slip angles, *i.e.*, the deviations from $\beta_1 = 0^\circ$ and $\beta_2 = 90^\circ$, thus determines the twist angles at the inner and outer walls. As shown in Fig. 2 and Fig. S1 (ESI†), the slip angles get larger as the shell gets thinner. Additionally, the larger the ratio K_{24}/K_2 is, the larger the value of $\Delta\beta = |\beta_2 - \beta_1|$ becomes (see the ESI†).

The bend deformation significantly affects the shape of a twist angle profile $\beta(\rho)$. As shown in Fig. 2, for thick shells, the twist angle increases slowly at small ρ then the slope gets steeper as ρ increases. This behavior results from the fact that the slow increase of $\beta(\rho)$ at small ρ can avoid the expensive bending energy with the small radius of curvature. We can expect that the increase of K_3 with fixed K_2 and K_{24} strengthens the nonlinearity of the twist angle profile (see the ESI†). In contrast, thin shells are far from the center of the cylinder, and the directors do not need to twist with high curvature. Thus $\beta(\rho)$ increases more linearly with ρ as in a planar twisted nematic cell.

Lastly, we should address one caveat that our calculations so far are based on the ansatz, eqn (2), and this case, *i.e.*, $K_{24} > 2K_2$, which violates the Ericksen inequalities should be dealt with a further discussion.[47–50] Generally, with the large saddle-splay elasticity, the free energy can have no lower bound, which predicts very strongly deformed patterns. Thus the scheme of the calculus of variation utilizing the Euler–Lagrange equations to find the energy minimum may make no sense. However, it is reported that the stabilization of deformations by non-linear higher order elasticity can be assumed to accommodate a weakly deformed director configuration and the large K_{24} violating the Ericksen inequalities, then the use of the Euler–Lagrange equation can be justified as in our calculations.[50]

Experiments

Polarized optical microscopy (POM) of a cylindrical shell of a nematic LCLC hints at the double-twist configuration predicted by the previous theoretical calculations based on the large K_{24} of LCLCs. As shown in Fig. 3(b), the cylindrical nematic LC shell formed in the nematic–isotropic coexistence phase looks bright under crossed polarizers of which the directions are either parallel or perpendicular to the capillary axis. Note that the interface between an isotropic core and the nematic shell is barely seen in Fig. 3(a) because the shell is very thin. We controlled the shell thickness by the temperature of the coexistence phase. Because two different handednesses are possible

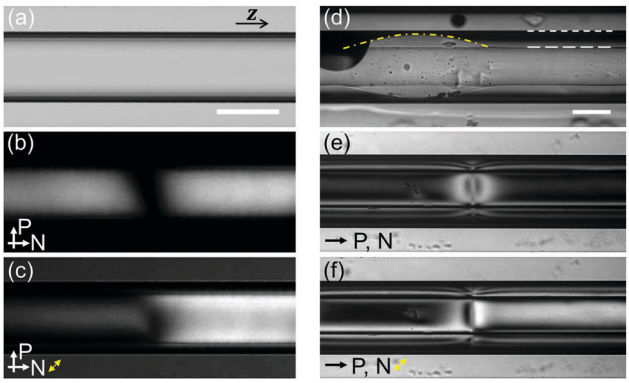

Fig. 3 Optical microscopy images of cylindrical nematic LC shells. (a) A bright-field microscopy image of 14.0% (wt/wt) DSCG at the nematic–isotropic coexistence phase of 29.5 °C. (b and c) POM images of the cylindrical shell in (a) between a polarizer (P) and an analyzer (N) with and without a full-wave plate under quasi-monochromatic illumination of wavelength 660 nm. The pass axis directions of the polarizers are shown as single-headed arrows, and the slow axis of the waveplate is shown as a double-headed arrow. (d) A bright-field microscopy image of a gel-coated glass rod located in the middle of a capillary tube. The white short- and long-dashed lines designate the wall of the capillary tube and the glass rod, respectively. The yellow short dash-dotted curve shows the boundary of a destabilized silicone gel drop wrapping around the glass rod. (e and f) POM images of 12.0% (wt/wt) nematic DSCG filling the gap between the rod and the tube at 23.0 °C. Note that they were taken in a coating-free and clean region of the glass rod under the same quasi-monochromatic illumination of wavelength 660 nm. Scale bars: 100 μm.

in the double-twist configuration, there should be a domain-wall-like defect between two adjacent domains of different handednesses, shown as the dark band of Fig. 3(b).[40,41] A full-wave plate inserted between the sample and the analyzer distinguishes the difference in handedness, as shown in Fig. 3(c).

Although the spontaneous growth of the nematic phase from the capillary wall is a handy way to make the nematic LC shell, it is not suitable for quantitative characterization and comparison with the numerical results because of the following. First, the elastic moduli and birefringence Δn of the nematic phase in the nematic–isotropic coexistence phase are not available in the literature and difficult to measure. This makes a quantitative analysis of POM images difficult. Second, the cylindrical core–shell structures formed by the nematic–isotropic coexistence phase are prone to Plateau–Rayleigh instability, *i.e.*, breaking up into droplets. Therefore, the core–shell structure, especially a thick nematic shell and a thin isotropic thread, does not stay stable for a long enough time, which is required for the nematic directors to equilibrate. For example, for 14.0% (wt/wt) nematic DSCG at room temperature, we have the director relaxation time scale $\tau \sim \eta d^2/K \sim 10^3$ s, where $\eta \sim 10$ Pa s is the twist viscosity and $d \sim 10$ μm is the typical length of the nematic shell. $K \sim 1$ pN is the twist elastic constant.[35] This implies that only thin shells barely have enough time to reach the equilibrium director configuration.

For the quantitative examination of the director configurations and their comparison with the numerical results, we developed an experimental method to make the stable nematic

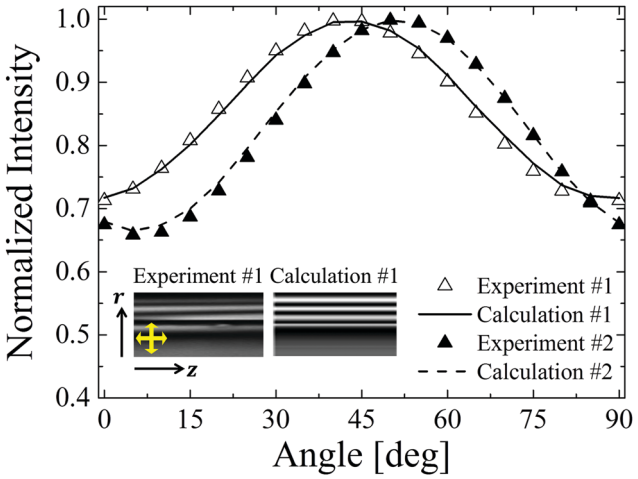

Fig. 4 Characterization of the double-twist director configuration using the transmitted light intensities. Normalized intensities of the transmitted light through the central region of the cylindrical shell is shown as a function of the angle between the polarizer and the analyzer. The filled and empty symbols are data from two representative domains on the left and right sides of a domain-wall-like defect in the double-twist director configuration of 14.0% (wt/wt) nematic DSCG in the cylindrical shell. The standard deviation of the intensity from the central region, *i.e.*, a rectangle spanning up to 3% of the cylinder diameter, is smaller than the height of the symbols. The two domains are supposed to have the same $|\beta_1|$ and $|\beta_2|$ of the opposite signs because they have opposite handedness of twist resulting in the topological defect between them. The solid and dashed curves are best fits to the data using the Jones calculus calculation. The inset compares the experimental POM image with the simulated optical texture from the best fit.

LC shell by locating a glass rod in the middle of the cylindrical capillary. Fig. 3(d) shows a suspending rod in a capillary tube. Fig. 3(e and f) are POM images of the cylindrical nematic LC shell between the rod and the tube, also with a domain-wall-like defect in the middle. Note that the POM images were taken from the silicone gel-free region, and the thicker shell exhibits a stripe pattern in the shell region implying multiple occurrence of 2π phase retardation of the quasi-monochromatic illumination.[6] The geometry of the double-twist configuration of the cylindrical shell makes the stripes parallel to the cylindrical axis; the optical path length of the transmitted light through the LC changes continuously along the radial direction when the capillaries are observed as in Fig. 3, and the nematic directors along the beam path also change in a complicated way.

To characterize the director configuration, we performed a quantitative POM analysis. Under quasi-monochromatic illumination at 660 nm, the capillary sample is placed between a polarizer and an analyzer with the polarization axis of both polarizers initially parallel to the capillary axis. While we rotated the polarizer and analyzer in the opposite directions with 5-degree steps until both polarizers align perpendicular to the capillary axis, we sequentially measured the transmitted light intensity through the central region of the capillary. The central region is set to be a rectangle spanning up to 3% of the cylinder diameter. Fig. 4 shows representative intensity profiles as a function of the angle between the polarizer and the analyzer: 14.0% (wt/wt) nematic DSCG shell of $\rho_1 = 0.5$. Two representative curves are taken from the left and right sides of a domain-wall-like defect and they are expected to have twist angles of the opposite signs but the same magnitudes.

To determine Δn, $\beta(\rho_1) = \beta_1$, and $\beta(\rho_2 = 1) = \beta_2$ from the experimental intensity profiles, we compared the experimental profiles with numerically generated profiles. Note that we generated the intensity profiles under the assumption that the twist angle changes linearly with respect to ρ from β_1 to β_2; the numerical calculation suggests that $\beta(\rho)$ for thin shells of $\rho_1 > 0.5$ is fairly linear as shown in Fig. 2. The best matching Δn, β_1, and β_2 show a good agreement with our theoretical predictions and the reported birefringence. For example, the four different intensity profiles of the 14.0% (wt/wt) nematic DSCG shell of $\rho_1 = 0.5$ give $|\beta_1| = 7.5 \pm 1.7^\circ$, $|\beta_2| = 71.5 \pm 1.5^\circ$, and $\Delta n \approx -0.015$. They are close to the theoretically predicted values $|\beta_1| = 3.2^\circ$ and $|\beta_2| = 68.3^\circ$, namely the solution of eqn (3) and (4) for a nematic DSCG shell of $\rho_1 = 0.5$, $k_2 = 1/30$, and $k_{24} = 1/2$. The Δn is also close to the literature value.[51] For 12.0% (wt/wt) nematic DSCG shells, we measured $|\beta_1| = 1.3 \pm 0.5^\circ$, $|\beta_2| = 83.3 \pm 2.4^\circ$, and $\Delta n \approx -0.014$, which are comparable with $|\beta_1| = 1.8$ and $|\beta_2| = 76.7^\circ$ resulting from $k_2 = 1/40$ and $k_{24} = 0.7^\circ$.

Conclusions

We have realized cylindrical nematic LC shells and investigated the double-twist director configuration therein resulting from the large saddle-splay elasticity. Under degenerate planar anchoring conditions at both the inner and outer interfaces of the cylindrical shell, the saddle-splay elasticity induces curvature-dependent azimuthal anchoring, and the LC sandwiched between two cylindrical interfaces exhibits the double-twist director configuration. The energetics regarding twist and bend elasticity and the shell thickness has been examined theoretically, and the theoretical calculations show a good agreement with experimentally measured twist angles. Per the shell preparation, we discovered and utilized the preferential wetting of the nematic phase on the capillary wall in the nematic–isotropic coexistence phase. Additionally, avoiding the Plateau–Rayleigh instability of the cylindrical liquid–liquid interface and the uncertainty in the elastic constants and birefringence, we introduce a way to prepare the cylindrical shell using a coaxial rod in a tube.

Looking forward, we think this cylindrical shell geometry can serve as novel confinement to other condensed matter including other LC phases, *e.g.*, cholesteric phase. Because it accommodates different curvatures, *i.e.*, concave or convex and along the circumference or the axis, we may expect unusual structures and topological defects. Furthermore, as in the spherical shell, the independently controllable boundary conditions at two interfaces enable us to explore various director configurations and topological defects.

Conflicts of interest

There are no conflicts to declare.

Acknowledgements

The authors gratefully acknowledge financial support from the Korean National Research Foundation through NRF-2015R1A2A2A01007613 and IBS-R020-D1. J. J. also acknowledges partial support from the 2015 Research Fund (1.150047.01) of UNIST (Ulsan National Institute of Science and Technology). Lastly, the authors thank the anonymous reviewer who pointed out the non-trivial physics behind adopting weak director deformations for large K_{24} violating Ericksen inequalities.

References

1 G. P. Crawford and S. Žumer, *Liquid crystals in complex geometries: formed by polymer and porous networks*, Taylor & Francis, 1996, p. 505.
2 F. Serra, *Liq. Cryst.*, 2016, **43**, 1920–1936.
3 C. Williams, P. Pierański and P. E. Cladis, *Phys. Rev. Lett.*, 1972, **29**, 90–92.
4 P. Cladis and M. Kléman, *J. Phys.*, 1972, **33**, 591–598.
5 R. Ondris-Crawford, E. P. Boyko, B. G. Wagner, J. H. Erdmann, S. Žumer and J. W. Doane, *J. Appl. Phys.*, 1991, **69**, 6380–6386.
6 P. S. Drzaic, *Liquid Crystal Dispersions*, World Scientific, 1995.
7 O. D. Lavrentovich, *Liq. Cryst.*, 1998, **24**, 117–126.
8 A. Fernández-Nieves, D. R. Link, M. Márquez and D. A. Weitz, *Phys. Rev. Lett.*, 2007, **98**, 087801.
9 T. Lopez-Leon and A. Fernandez-Nieves, *Colloid Polym. Sci.*, 2011, **289**, 345–359.
10 J. Jeong and M. Won Kim, *Appl. Phys. Lett.*, 2012, **101**, 061914.
11 J. Jeong and M. W. Kim, *Phys. Rev. Lett.*, 2012, **108**, 207802.
12 E. Pairam, J. Vallamkondu, V. Koning, B. C. van Zuiden, P. W. Ellis, M. A. Bates, V. Vitelli and A. Fernandez-Nieves, *Proc. Natl. Acad. Sci. U. S. A.*, 2013, **110**, 9295–9300.
13 M. Urbanski, C. G. Reyes, J. Noh, A. Sharma, Y. Geng, V. Subba Rao Jampani and J. P. F. Lagerwall, *J. Phys.: Condens. Matter*, 2017, **29**, 133003.
14 T. C. Lubensky, D. Pettey, N. Currier and H. Stark, *Phys. Rev. E: Stat. Phys., Plasmas, Fluids, Relat. Interdiscip. Top.*, 1998, **57**, 610–625.
15 P. Poulin, H. Stark, T. C. Lubensky and D. A. Weitz, *Science*, 1997, **275**, 1770–1773.
16 P. Poulin and D. A. Weitz, *Phys. Rev. E: Stat. Phys., Plasmas, Fluids, Relat. Interdiscip. Top.*, 1998, **57**, 626–637.
17 U. Tkalec, M. Ravnik, S. Copar, S. Zumer and I. Musevic, *Science*, 2011, **333**, 62–65.
18 B. Senyuk, Q. Liu, S. He, R. D. Kamien, R. B. Kusner, T. C. Lubensky and I. I. Smalyukh, *Nature*, 2012, **493**, 200–205.
19 I. Muševič, *Liquid crystal colloids*, Springer, 2017.
20 V. Vitelli and D. R. Nelson, *Phys. Rev. E: Stat., Nonlinear, Soft Matter Phys.*, 2006, **74**, 021711.
21 A. Fernández-Nieves, V. Vitelli, A. S. Utada, D. R. Link, M. Márquez, D. R. Nelson and D. A. Weitz, *Phys. Rev. Lett.*, 2007, **99**, 157801.
22 H. Shin, M. J. Bowick and X. Xing, *Phys. Rev. Lett.*, 2008, **101**, 037802.
23 T. Lopez-Leon and A. Fernandez-Nieves, *Phys. Rev. E: Stat., Nonlinear, Soft Matter Phys.*, 2009, **79**, 021707.
24 T. Lopez-Leon, V. Koning, K. B. S. Devaiah, V. Vitelli and A. Fernandez-Nieves, *Nat. Phys.*, 2011, **7**, 391–394.
25 T. Lopez-Leon, A. Fernandez-Nieves, M. Nobili and C. Blanc, *Phys. Rev. Lett.*, 2011, **106**, 247802.
26 H.-L. Liang, S. Schymura, P. Rudquist and J. Lagerwall, *Phys. Rev. Lett.*, 2011, **106**, 247801.
27 H.-L. Liang, R. Zentel, P. Rudquist and J. Lagerwall, *Soft Matter*, 2012, **8**, 5443.
28 H.-L. Liang, J. Noh, R. Zentel, P. Rudquist and J. P. F. Lagerwall, *Philos. Trans. R. Soc., A*, 2013, **371**, 20120258.
29 Y. Uchida, Y. Takanishi and J. Yamamoto, *Adv. Mater.*, 2013, **25**, 3234–3237.
30 A. Darmon, M. Benzaquen, D. Seč, S. Čopar, O. Dauchot and T. Lopez-Leon, *Proc. Natl. Acad. Sci. U. S. A.*, 2016, **113**, 9469–9474.
31 L. Tran, M. O. Lavrentovich, G. Durey, A. Darmon, M. F. Haase, N. Li, D. Lee, K. J. Stebe, R. D. Kamien and T. Lopez-Leon, *Phys. Rev. X*, 2017, **7**, 041029.
32 V. Koning, B. C. van Zuiden, R. D. Kamien and V. Vitelli, *Soft Matter*, 2014, **10**, 4192–4198.
33 L. Tortora and O. D. Lavrentovich, *Proc. Natl. Acad. Sci. U. S. A.*, 2011, **108**, 5163–5168.
34 S. Zhou, Y. A. Nastishin, M. M. Omelchenko, L. Tortora, V. G. Nazarenko, O. P. Boiko, T. Ostapenko, T. Hu, C. C. Almasan, S. N. Sprunt, J. T. Gleeson and O. D. Lavrentovich, *Phys. Rev. Lett.*, 2012, **109**, 037801.
35 S. Zhou, K. Neupane, Y. A. Nastishin, A. R. Baldwin, S. V. Shiyanovskii, O. D. Lavrentovich and S. Sprunt, *Soft Matter*, 2014, **10**, 6571–6581.
36 J. Jeong, Z. S. Davidson, P. J. Collings, T. C. Lubensky and A. G. Yodh, *Proc. Natl. Acad. Sci. U. S. A.*, 2014, **111**, 1742–1747.
37 J. Jeong, L. Kang, Z. S. Davidson, P. J. Collings, T. C. Lubensky and A. G. Yodh, *Proc. Natl. Acad. Sci. U. S. A.*, 2015, **112**, E1837–E1844.
38 K. Nayani, J. Fu, R. Chang, J. O. Park and M. Srinivasarao, *Proc. Natl. Acad. Sci. U. S. A.*, 2017, **114**, 3826–3831.
39 J. Fu, K. Nayani, J. O. Park and M. Srinivasarao, *NPG Asia Mater.*, 2017, **9**, e393.
40 Z. S. Davidson, L. Kang, J. Jeong, T. Still, P. J. Collings, T. C. Lubensky and A. G. Yodh, *Phys. Rev. E: Stat., Nonlinear, Soft Matter Phys.*, 2015, **91**, 050501.
41 K. Nayani, R. Chang, J. Fu, P. W. Ellis, A. Fernandez-Nieves, J. O. Park and M. Srinivasarao, *Nat. Commun.*, 2015, **6**, 8067.
42 S. Zhou, Y. A. Nastishin, M. M. Omelchenko, L. Tortora, V. G. Nazarenko, O. P. Boiko, T. Ostapenko, T. Hu, C. C. Almasan, S. N. Sprunt, J. T. Gleeson and O. D. Lavrentovich, *Phys. Rev. Lett.*, 2012, **109**, 037801.
43 J. Lydon, *Curr. Opin. Colloid Interface Sci.*, 2004, **8**, 480–490.
44 V. Duclaux, C. Clanet and D. Quéré, *J. Fluid Mech.*, 2006, **556**, 217.
45 P. Yeh and C. Gu, *Optics of liquid crystal displays*, Wiley, 2010, p. 770.
46 R. J. Ondris-Crawford, G. P. Crawford, S. Zumer and J. W. Doane, *Phys. Rev. Lett.*, 1993, **70**, 194–197.

47 J. L. Ericksen, *Phys. Fluids*, 1966, **9**, 1205–1207.
48 V. M. Pergamenshchik, *Phys. Rev. E: Stat. Phys., Plasmas, Fluids, Relat. Interdiscip. Top.*, 1993, **48**, 1254–1264.
49 V. M. Pergamenshchik, *Phys. Rev. E: Stat. Phys., Plasmas, Fluids, Relat. Interdiscip. Top.*, 1998, **58**, R16–R19.
50 G. Barbero and V. M. Pergamenshchik, *Phys. Rev. E: Stat., Nonlinear, Soft Matter Phys.*, 2002, **66**, 051706.
51 Y. A. Nastishin, H. Liu, T. Schneider, V. Nazarenko, R. Vasyuta, S. V. Shiyanovskii and O. D. Lavrentovich, *Phys. Rev. E: Stat., Nonlinear, Soft Matter Phys.*, 2005, **72**, 041711.